



This is the peer reviewed version of the following article:

Gao, N., Geyer, F., Pilat, D. W., Wooh, S., Vollmer, D., Butt, H.-J., et al. (2018). How drops start sliding over solid surfaces. *Nature Physics*, 14(2), 191-196. doi:10.1038/NPHYS4305.

, which has been published in final form at: [10.1038/NPHYS4305](https://doi.org/10.1038/NPHYS4305)

## **How drops start sliding over solid surfaces**

Nan Gao, Florian Geyer, Dominik W. Pilat, Sanghyuk Wooh, Doris Vollmer, Hans-Jürgen Butt & Rüdiger Berger

# How drops start sliding over solid surfaces

1  
2  
3  
4  
5  
6  
7  
8  
9  
10  
11  
12  
13  
14  
15  
16  
17  
18  
19  
20  
21  
22  
23

Nan Gao<sup>1,2\*</sup>, Florian Geyer<sup>1</sup>, Dominik W. Pilat<sup>1</sup>, Sanghyuk Wooh<sup>1</sup>, Doris Vollmer<sup>1</sup>, Hans-Jürgen Butt<sup>1</sup>, Rüdiger Berger<sup>1\*</sup>

1 Max Planck Institute for Polymer Research, Ackermannweg 10, 55128 Mainz, Germany

2 Fudan University, 220 Handan Road, Shanghai 200433, People’s Republic of China

\* Email: nann.gao@gmail.com

\* Email: berger@mpip-mainz.mpg.de

24 **It has been known for more than 200 years that the maximum static friction force between**  
25 **two solid surfaces is usually greater than the kinetic friction force. In contrast to solid–solid**  
26 **friction, there is a lack of understanding of liquid–solid friction, i.e. the forces that impede**  
27 **the lateral motion of a drop of liquid on a solid surface. Here, we report that the lateral**  
28 **adhesion force between a liquid drop and a solid can be divided into a static and a kinetic**  
29 **regime. This striking analogy with solid–solid friction is a generic phenomenon that holds**  
30 **for liquids of different polarities and surface tensions on smooth, rough and structured**  
31 **surfaces.**

32  
33 When two solid objects are brought into contact, a threshold force  $F_{\text{THRD}}$  must be overcome in  
34 order for one of the objects to slide<sup>1-3</sup>. This phenomenon can be visualised in a typical  
35 classroom experiment where a solid block attached to a spring is pulled over a solid surface  
36 (Fig. 1a). The static force  $F_S$  is applied to the stationary block and then increased until it  
37 exceeds  $F_{\text{THRD}}$ , upon which the block begins to slide. After that, a lower kinetic force  $F_{\text{KIN}}$  is  
38 required to maintain the block’s motion<sup>3</sup>. However, it is not clear whether these forces  
39 develop in a comparable manner when a drop of liquid resting on a solid surface starts to slide.  
40 This gap in our understanding is astonishing, given the fact that liquid drops are omnipresent  
41 in our lives and their motion is relevant for numerous applications, including microfluidics<sup>4</sup>,  
42 printing<sup>5</sup>, condensation<sup>6,7</sup>, and water collection<sup>8,9</sup>. Hence insight on the behaviour of drops  
43 that start sliding over solid surfaces is needed.

44 A sessile drop of liquid is usually in molecular contact with the supporting solid surface. In  
45 contrast, two solid bodies are in direct contact only at asperities owing to surface  
46 roughness<sup>10,11</sup>. Thus, the real contact area of a solid–solid contact is much smaller than the  
47 apparent contact area. Consequently the sliding of drops might be fundamentally different.  
48 However, by simply observing a drop of water on a pivot window pane, we know that also  
49 sessile drops start sliding when a critical tilt angle is reached, i.e. when the gravitational force  
50 acting on the drop overcomes the lateral adhesion force. The question may therefore be  
51 raised whether a static and a kinetic regime are also present for sessile drops. The general  
52 question is: How do drops start sliding over solid surfaces and how do the forces develop  
53 while the drops slide?

Owing to higher gravitational forces, larger drops start sliding at lower tilt angles. Sliding is opposed by capillary forces. They are associated with a contact angle difference between the rear and the front of the drop. Indeed, the interactions between solid surfaces and liquids are described by the liquid–air surface tension  $\gamma$  and the apparent rear and front contact angles of the drop,  $\theta_{\text{Rear}}$  and  $\theta_{\text{Front}}$ , respectively. Thus, the surface tension, the contact angles and the drop contact width  $L$  determine the lateral adhesion force  $F_{\text{LA}}$  by<sup>12-16</sup>

$$F_{\text{LA}} = k \cdot L \cdot \gamma \cdot (\cos \theta_{\text{Rear}} - \cos \theta_{\text{Front}}). \quad \text{Eq. (1)}$$

The dimensionless factor  $k$  accounts for the precise shape of the solid–liquid–air three-phase contact line of the drop. Values for  $k$  were calculated to be between  $1/2$  and  $\pi/2$ .<sup>12,17-19</sup>

Despite the omnipresence of drops, the onset of motion has never been correlated with the development of lateral adhesion forces. The lateral adhesion force has been related to external forces that cause a drop to slide, such as gravitational<sup>20,21</sup>, centrifugal<sup>22</sup>, magnetic<sup>23</sup>, or capillary forces<sup>24-26</sup>. The contact angles have also been experimentally and numerically investigated for the pinned state, i.e. just before and during steady motions<sup>27,28</sup>. However, once a drop has started to slide, the lateral adhesion force cannot be tracked using simple techniques. Astonishingly, it is unclear how the force develops and how it depends on sliding velocity. We will demonstrate that, for the lateral liquid–solid adhesion, we can distinguish a static and a kinetic regime, analogous to solid–solid friction.

In order to measure the lateral adhesion force between a drop of liquid and a solid substrate, a capillary is positioned in the centre of the drop. The substrate with the drop is moved sideways against the capillary at a constant velocity. When the capillary reaches the edge of the drop, it sticks to the drop. Consequently the motion of the substrate is accompanied by a deformation of the drop as well as a deflection of the capillary. Initially, the drop remains pinned to the substrate (Fig. 1b). Once the capillary exerts a certain critical force, the drop overcomes the lateral adhesion and is set into translational motion relative to the substrate, i.e. the front and rear side of the drop start moving. The deflection  $D$  of the capillary is measured by recording the position of a reflected laser beam with a position-sensitive detector<sup>25</sup>. Then, the lateral adhesion force acting on the drop can be calculated by  $F_{\text{LA}} = \kappa \cdot D$ , where  $\kappa$  is the spring constant of the capillary. Simultaneously, the drop’s shape is monitored by two cameras, which are synchronised with the force measurement. In this way the lateral

84 adhesion force can be correlated with the contact angles. Velocities ranged from 1  $\mu\text{m/s}$  to 50  
85  $\text{mm/s}$  (see methods section).

86 As a representative example we start with a drop of an ionic liquid placed on a fluorinated Si  
87 wafer. It forms a contact angle of  $\approx 70^\circ$ . Moving the wafer laterally increased the force (blue  
88 circles in Fig. 2a) until a maximum force of 50  $\mu\text{N}$  was reached (after 11 s). This maximum force  
89 corresponded to the threshold force for the drop, upon which it started to slide. Then the  
90 force subsequently decreased to a constant level of  $\approx 33 \mu\text{N}$ , which was only 66% of the  
91 maximal force (after 17 s). Accordingly, we distinguish a static, a transition, and a kinetic  
92 regime shown in different shades of green in Fig. 2a. The presence of a higher threshold force  
93 compared to the force required for continuous motion explains the manner a drop slides  
94 downhill in a tilted-plate experiment. It is analogous to solid–solid friction, where a solid object  
95 placed on a tilted plane keeps sliding once the static friction threshold force has been  
96 overcome<sup>29,30</sup>. Initially, the contact line of the drop was pinned and the contact width and  
97 length remained constant at about 2.3 mm (Fig. 2b, first 5 s). Meanwhile, the front and rear  
98 contact angles increased and decreased, respectively, as the drop deformed (Fig. 2c). After 5  
99 – 8 s, the contact line started reforming, resulting in a longer and narrower drop shape. After  
100 about 10 s, the contact angles reached a maximum value of  $\approx 86^\circ$  at the front and a minimum  
101 of  $\approx 43^\circ$  at the rear. At this point of maximum contact angle difference of  $\approx 40^\circ$ , the static  
102 adhesion force reached its maximum, which constituted the threshold force of the  
103 translational motion. In the transition regime, the contact length decreased continuously. The  
104 rear contact angle increased by more than  $10^\circ$ , whereas the front contact angle decreased by  
105  $\approx 5^\circ$  over time. Finally a kinetic regime was reached (after  $\approx 18$  s), which was characterized by  
106 constant lateral adhesion forces, constant contact angles, constant contact widths and contact  
107 lengths.

108 We then took the measured contact widths (Fig. 2b) and the contact angles (Fig. 2c) to  
109 calculate the lateral adhesion force using Eq. 1. Thereby we simplified Eq. 1 by assuming a  
110 constant value of  $k = 1$  thus disregarding shape changes of the drop contour and variations of  
111 the contact angle along the contour<sup>17</sup> (see Supplementary Material for a discussion of the  $k$   
112 factor and its temporal development). This calculation almost quantitatively agreed with the  
113 measured lateral adhesion force (red squares in Fig. 2a). In particular, the calculated lateral  
114 adhesion force reproduced the transition between the static and kinetic regimes. Once the

115 threshold adhesion force  $F_{\text{THRD}}$  has been overcome, the drop transitions from a static regime  
 116 to a steady kinetic regime. Consequently, the liquid–solid adhesion forces in the static and  
 117 kinetic regimes are substantially different, owing to different contact angles and contact  
 118 widths in these two regimes:

$$119 \quad F_S = \gamma \cdot L_S \cdot (\cos \theta_S^{\text{Rear}} - \cos \theta_S^{\text{Front}}) \quad (\text{Eq. 2a})$$

$$120 \quad F_{\text{KIN}} = \gamma \cdot L_{\text{KIN}} \cdot (\cos \theta_{\text{KIN}}^{\text{Rear}} - \cos \theta_{\text{KIN}}^{\text{Front}}) \quad (\text{Eq. 2b})$$

121 Here,  $F_S$ ,  $L_S$ ,  $\theta_S^{\text{Front}}$  and  $\theta_S^{\text{Rear}}$  are the lateral adhesion force, contact width, and front and rear  
 122 contact angles in the static (S) regime.  $F_{\text{KIN}}$ ,  $L_{\text{KIN}}$ ,  $\theta_{\text{KIN}}^{\text{Front}}$  and  $\theta_{\text{KIN}}^{\text{Rear}}$  are the lateral adhesion force,  
 123 contact width, and front and rear contact angles in the kinetic (KIN) regime.

124 To verify whether the discrimination between static and kinetic lateral adhesion forces is a  
 125 generic feature, we analysed a number of different liquid–solid combinations (Fig. 3). We used  
 126 water and hexadecane in addition to a non-volatile ionic liquid (1-butyl-2,3-  
 127 dimethylimidazolium bis(trifluoromethanesulfonyl)imide). The solid surfaces include  
 128 superhydrophobic silicone nanofilaments (SNFs), silicon wafers (Si), SU-8 micropillar arrays,  
 129 multilayers of titanium dioxide nanoparticles ( $\text{TiO}_2$ ) and cross-linked polydimethylsiloxane  
 130 (PDMS) substrates (Supplementary Fig. 1). All samples were homogenous at the scale of the  
 131 drop radius and did not have distinct pinning centers. For all liquid–solid combinations we  
 132 observed a static, a transition and a kinetic regime (Fig. 3a, Supplementary Figs. 5-10). It  
 133 should be noted that the lateral adhesion force in the kinetic regime never exceeded the  
 134 threshold force (Fig. 3a). Thus

$$135 \quad F_{\text{THRD}} \geq F_{\text{KIN}} \quad (\text{Eq. 3})$$

136 Notably,  $F_{\text{THRD}} = F_{\text{KIN}}$  is possible, too<sup>25</sup>. Surfaces coated with brushes of liquid like  
 137 poly(dimethylsiloxane) (PDMS) showed  $F_{\text{THRD}} = F_{\text{KIN}}$ . The reason is that these surfaces  
 138 hardly show any contact angle hysteresis for water<sup>31</sup>, i.e.  $\cos \theta^{\text{Rear}} \approx \cos \theta^{\text{Front}}$   
 139 (Supplementary Fig. 11).

140 Furthermore, good agreement between calculated and measured lateral adhesion forces was  
 141 observed for various wetting scenarios, including hexadecane and ionic liquid on fluorinated  
 142 silicon wafers, and water on superhydrophobic surfaces (silicone nanofilaments and  
 143 fluorinated SU-8 pillars), where drops partially rested on air cushions. The differences in

144 adhesion between the drops and the substrates resulted in different apparent contact angles  
145 and contact widths among the liquid–solid combinations (Supplementary Figs. 5–10). We  
146 attribute the small discrepancies between calculated and measured lateral adhesion forces to  
147 microscopic distortions of the three-phase contact lines<sup>30</sup>. The latter can be accounted for by  
148 the  $k$  factor (Supplementary Figs. 5-10 and Supplementary Table 1). Indeed, the  $k$  factor of our  
149 measurements lies between 0.25 and 4. It is worth emphasizing that the  $k$  factor changed  
150 continuously while the drop passed from the static to the kinetic regime. These observations  
151 indicate that a constant  $k$  factor is not sufficient to describe how drops slide over a solid  
152 surface. In particular for large scale heterogeneous surfaces that exhibit distinct pinning  
153 centers,  $F_{\text{KIN}}$  occasionally exceeded  $F_{\text{THRD}}$  (Supplementary Fig. 12 and Griffiths et. al.<sup>32</sup>). Thus,  
154 the lateral adhesion force provides quantitative information on the homogeneity or  
155 cleanliness of a surface.

156 In order to compare the different liquid–solid combinations independently from drop size, we  
157 calculated the static and lateral adhesion force per unit width (Fig. 3b). This analysis yielded  
158 values ranging from 2  $\mu\text{N}/\text{mm}$  to 110  $\mu\text{N}/\text{mm}$ . The increasing lateral adhesion force per unit  
159 width depends on the interplay between surface tension and contact angle hysteresis. In  
160 addition, we calculated the ratios of the kinetic force divided by the static threshold force. For  
161 all different liquid–solid combinations, we obtained a ratio of  $F_{\text{KIN}}/F_{\text{THRD}} \leq 1$  (Fig. 3c).

162 In general, contact angles depend on the sliding velocity.<sup>33</sup> Therefore we measured  $F_{\text{KIN}}$  and  
163  $F_{\text{THRD}}$  for increasing sliding velocities in a velocity range from  $10^{-3}$  to 22 mm/s for hexadecane  
164 on a Silicon wafer surface (filled symbols in Fig. 4a-b). We found that  $F_{\text{KIN}}$  and  $F_{\text{THRD}}$  are  
165 relatively constant up to a  $\text{Ca}$  of  $10^{-5}$ . Then they increase with velocity. Furthermore, the  
166 dependence and magnitude of the measured forces are in agreement with the forces  
167 calculated by the front and rear contact angles (Fig. 4c) using equation 1 (open symbols in Fig.  
168 4a-b). Perrin et al. measured the dynamic macroscopic contact angle of a silicon wafer  
169 withdrawn from a silicone oil bath<sup>34</sup>. These experiments revealed a strong change in the  
170 cosines of the contact angles between  $10^{-5} < \text{Ca} < 10^{-3}$ . This region marked the transition from  
171 energy dissipation dominated by defects to viscous dissipation. Our measured increase in  $F_{\text{KIN}}$   
172 falls in this regime and therefore we attribute the increase of  $F_{\text{KIN}}$  at  $\text{Ca} > 10^{-5}$  to viscous  
173 dissipation in addition to thermally activated process at the contact line. The increase in  $F_{\text{KIN}}$   
174 falls in this regime, and therefore we attribute the increase of  $F_{\text{KIN}}$  at  $\text{Ca} > 10^{-5}$  to viscous

175 dissipation in addition to thermally activated processes at the contact line. The latter was  
176 discussed as a result of a rugged energy landscape of the sample surface leading to a thermally  
177 activated process of the contact line dynamics.<sup>34</sup> In our measurements, we could not resolve  
178 a logarithmic dependence of  $F_{KIN}$  and  $F_{THRD}$  at  $Ca < 10^{-5}$  which would have given insight into  
179 such thermally activated process of the moving liquid. In particular, we found that the ratio of  
180  $F_{KIN}/F_{THRD} \leq 1$  within the probed velocity range (Supplementary Figure 13 and 14).

181 In order to study whether drop-solid friction scales with the contact line or with contact area,  
182 we varied the drop volume (Supplementary Fig. 13). This results in a variation of the contact  
183 area by a factor of  $> 4$ . The linear extrapolation of the kinetic force dependence suggests a  
184 linear dependence with an intercept slightly below zero force. Therefore we conclude that the  
185 liquid drop friction is dominated by contact line friction and interfacial friction only plays a  
186 minor role. This conclusion is supported by an estimation of the friction force contribution of  
187 a solid-liquid interface based on a Green-Kubo relation of Huang and Szlufarska<sup>35</sup> and by  
188 monitoring the motion of drops over the surfaces, showing that the motion is dominated by  
189 rolling (Supplementary Fig. 15, Movies 8-11). In contrast, contact line friction does not play a  
190 role for liquid-liquid interfaces such as drops on lubricated surfaces.<sup>36</sup>

191 As an example of a natural, structured surface, we measured the lateral adhesion of a water  
192 drop on a goose feather (Fig. 5). Again, we observed a static regime and a kinetic regime. The  
193 static threshold force was even 2.4 times larger than the average kinetic force required for the  
194 continuous motion of the water drop. In addition, the lateral adhesion force varied in the  
195 kinetic regime (Fig. 5b). Likely, these variations are related to the flexibility and the  
196 microscopic structures of the feather (Fig. 5c-d) which lead to a stick-slip motion of the drop.  
197 Energy is dissipated mainly by depinning from a few surface protrusions which shows no  
198 velocity dependence (Supplementary Fig. 16)<sup>37</sup>. The latter is in contrast to stick-slip motion of  
199 two solids.<sup>38,39</sup> Consequently, for such rough and elastic surfaces the contribution of viscous  
200 dissipation to the overall energy dissipation of the sliding drop is low. It is not clear what role  
201 such a stick-slip motion and the associated velocity independence play for the live of a goose  
202 in water. The constant and low kinetic force could potentially reduce energy losses at the  
203 three-phase contact line of the feather with water and air.

## 204 **Acknowledgement**



205 We thank G. Auernhammer, M. Bonn, N. Encinas, M. Kappl, T. Kajiyama, P. Papadopoulos,  
206 F. Schellenberger, W. Steffen, and D. Wang for stimulating discussions, and M. Bach, G. Glaser  
207 and G. Schäfer for technical support. This work was supported by the SPP 1420 (H.J. B.), ERC  
208 advanced grant 340391–SUPRO and SPP 8173 (D. V.). N.G. thanks the National Postdoctoral  
209 Science Foundation of China for the International Postdoctoral Fellowship, and S.W. thanks  
210 the Alexander von Humboldt Foundation for a postdoctoral fellowship. D.W.P. is grateful for  
211 funding from the German National Academic Foundation.

### 212 **Author contributions**

213 N.G. carried out the experiments and wrote the manuscript. D.W.P., R.B. and H.-J.B. designed  
214 and constructed the homebuilt setup. F.G. and S.W. prepared the solid surfaces. R.B., D.V.,  
215 N.G. and H.-J.B. contributed to the experimental planning, data analysis, and manuscript  
216 preparation. All authors reviewed and approved the manuscript.

### 217 **Additional information**

218 Supplementary information is available in the online version of this paper. Reprints and  
219 permissions information are available online at [www.....com/reprints](http://www.....com/reprints). Correspondence and  
220 requests for materials should be addressed to R.B., H.-J.B. or D.V.

221 **Data Availability Statement:** The data that support the plots within this paper and other  
222 findings of this study are available from the corresponding author upon request.

### 223 **Competing financial interests**

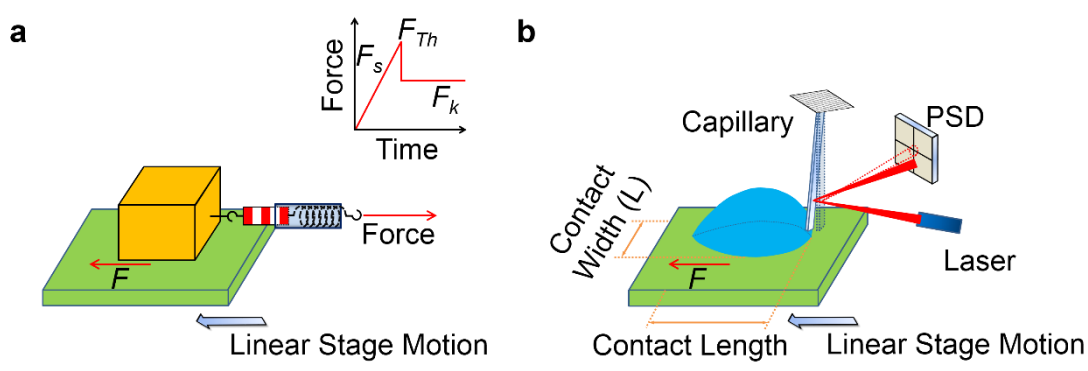
224 The authors declare no competing financial interests.

### 225 **References**

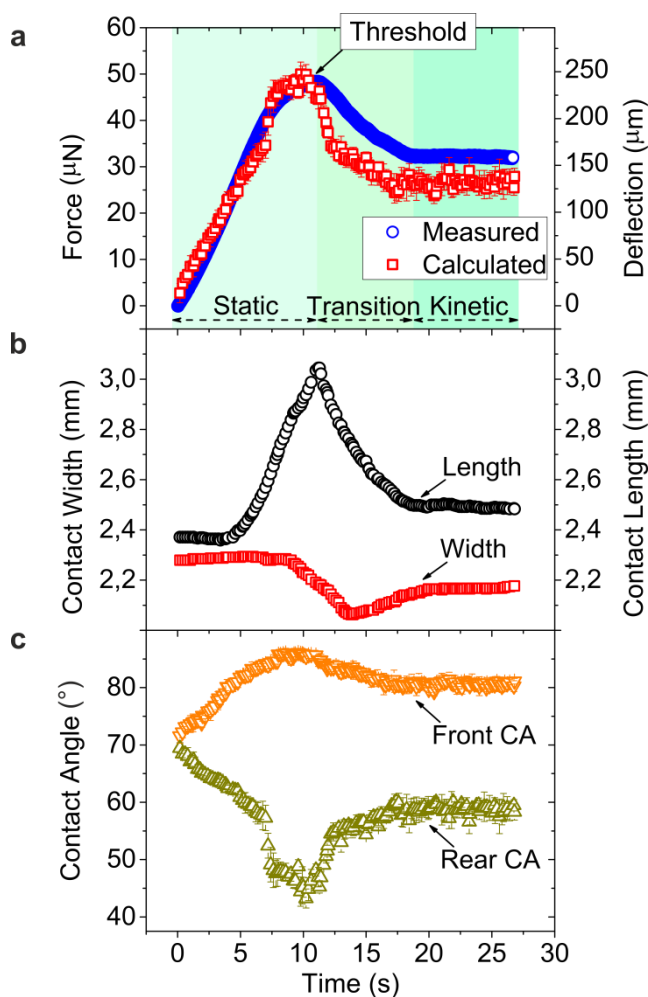
- 226 1 Archard, J. F. Contact and Rubbing of Flat Surfaces. *J. Appl. Phys.* **24**, 981-988, (1953).
- 227 2 Persson, B. T. in *Encyclopedia of Lubricants and Lubrication* (ed Theo Mang) Ch. 80, 791-797  
228 (Springer Berlin Heidelberg, 2014).
- 229 3 Butt, H.-J. & Kappl, M. *Friction*. (Wiley-VCH Verlag GmbH & Co. KGaA, 2010).
- 230 4 Shestopalov, I., Tice, J. D. & Ismagilov, R. F. Multi-step synthesis of nanoparticles performed  
231 on millisecond time scale in a microfluidic droplet-based system. *Lab Chip* **4**, 316-321, (2004).
- 232 5 Calvert, P. Inkjet Printing for Materials and Devices. *Chem. Mater.* **13**, 3299-3305, (2001).
- 233 6 Cheng, P., Quan, X., Gong, S., Liu, X. & Yang, L. in *Advances in Heat Transfer* Vol. 46 (eds Young  
234 I. Cho John P. Abraham Ephraim M. Sparrow & Gorman John M) 187-248 (Elsevier, 2014).
- 235 7 Rykaczewski, K. *et al.* Dropwise Condensation of Low Surface Tension Fluids on Omniphobic  
236 Surfaces. *Sci. Rep.* **4**, 4158; DOI:10.1038/srep04158, (2014).

- 237 8 Zheng, Y. *et al.* Directional water collection on wetted spider silk. *Nature* **463**, 640-643, (2010).
- 238 9 Park, K.-C., Chhatre, S. S., Srinivasan, S., Cohen, R. E. & McKinley, G. H. Optimal Design of
- 239 Permeable Fiber Network Structures for Fog Harvesting. *Langmuir* **29**, 13269-13277, (2013).
- 240 10 Bowden, F. P. & Tabor, D. *The Friction and Lubrication of Solids*. (Clarendon Press, 2001).
- 241 11 Bhushan, B., Israelachvili, J. N. & Landman, U. Nanotribology: friction, wear and lubrication at
- 242 the atomic scale. *Nature* **374**, 607-616, (1995).
- 243 12 Extrand, C. W. & Gent, A. N. Retention of liquid drops by solid surfaces. *J. Colloid Interface Sci.*
- 244 **138**, 431-442, (1990).
- 245 13 Brown, R. A., Orr Jr, F. M. & Scriven, L. E. Static drop on an inclined plate: Analysis by the finite
- 246 element method. *J. Colloid Interface Sci.* **73**, 76-87, (1980).
- 247 14 Extrand, C. W. & Kumagai, Y. Liquid Drops on an Inclined Plane: The Relation between Contact
- 248 Angles, Drop Shape, and Retentive Force. *J. Colloid Interface Sci.* **170**, 515-521, (1995).
- 249 15 Frenkel, Y. I. On the behaviour of drops of liquid on the surface of a solid. I. Sliding of drops on
- 250 an inclined plane. *J. Exp. Theor. Phys.* **18**, 658-667, (1948).
- 251 16 Kawasaki, K. Study of wettability of polymers by sliding of water drop. *J. Colloid Sci.* **15**, 402-
- 252 407, (1960).
- 253 17 ElSherbini, A. & Jacobi, A. Retention forces and contact angles for critical liquid drops on non-
- 254 horizontal surfaces. *J. Colloid Interface Sci.* **299**, 841-849, (2006).
- 255 18 Dussan, V. On the ability of drops to stick to surfaces of solids. Part 3. The influences of the
- 256 motion of the surrounding fluid on dislodging drops. *J. Fluid Mech.* **174**, 381-397, (1987).
- 257 19 Wolfram, E. & Faust, R. in *Wetting, Spreading, and Adhesion* (ed J. F. Padday) 213 (Academic
- 258 Press, 1978).
- 259 20 Antonini, C., Carmona, F. J., Pierce, E., Marengo, M. & Amirfazli, A. General Methodology for
- 260 Evaluating the Adhesion Force of Drops and Bubbles on Solid Surfaces. *Langmuir* **25**, 6143-
- 261 6154, (2009).
- 262 21 Berejnov, V. & Thorne, R. E. Effect of transient pinning on stability of drops sitting on an
- 263 inclined plane. *Phys. Rev. E* **75**, 066308, (2007).
- 264 22 Tadmor, R. *et al.* Measurement of Lateral Adhesion Forces at the Interface between a Liquid
- 265 Drop and a Substrate. *Phys. Rev. Lett.* **103**, 266101, (2009).
- 266 23 Timonen, J. V. I., Latikka, M., Ikkala, O. & Ras, R. H. A. Free-decay and resonant methods for
- 267 investigating the fundamental limit of superhydrophobicity. *Nat. Commun.* **4**:2398 DOI:
- 268 10.1038/ncomms3398, (2013).
- 269 24 Lagubeau, G., Le Merrer, M., Clanet, C. & Quere, D. Leidenfrost on a ratchet. *Nat. Phys.* **7**, 395-
- 270 398, (2011).
- 271 25 Pilat, D. W. *et al.* Dynamic Measurement of the Force Required to Move a Liquid Drop on a
- 272 Solid Surface. *Langmuir* **28**, 16812-16820, (2012).
- 273 26 't Mannetje, D. *et al.* Electrically Tunable Wetting Defects Characterized by a Simple Capillary
- 274 Force Sensor. *Langmuir* **29**, 9944-9949, (2013).
- 275 27 Olin, P., Lindström, S. B., Pettersson, T. & Wågberg, L. Water Drop Friction on
- 276 Superhydrophobic Surfaces. *Langmuir* **29**, 9079-9089, (2013).
- 277 28 Pierce, E., Carmona, F. J. & Amirfazli, A. Understanding of sliding and contact angle results in
- 278 tilted plate experiments. *Colloid Surf. A-Physicochem. Eng. Asp.* **323**, 73-82, (2008).
- 279 29 Sakai, M. *et al.* Direct Observation of Internal Fluidity in a Water Droplet during Sliding on
- 280 Hydrophobic Surfaces. *Langmuir* **22**, 4906-4909, (2006).
- 281 30 Semperebon, C. & Brinkmann, M. On the onset of motion of sliding drops. *Soft Matter* **10**, 3325-
- 282 3334, (2014).
- 283 31 Krumpfer, J. W. & McCarthy, T. J. Contact angle hysteresis: a different view and a trivial recipe
- 284 for low hysteresis hydrophobic surfaces. *Farad. Discuss.* **146**, 103-111, (2010).
- 285 32 Griffiths, P. R. *Static and Dynamic Components of Droplet Friction* Master of Science in
- 286 Mechanical Engineering thesis, University of South Florida, (2013).
- 287 33 Snoeijer, J. H. & Andreotti, B. Moving Contact Lines: Scales, Regimes, and Dynamical
- 288 Transitions. *Annu. Rev. Fluid Mech.* **45**, 269-292, (2013).

289 34 Perrin, H., Lhermerout, R., Davitt, K., Rolley, E. & Andreotti, B. Defects at the Nanoscale Impact  
 290 Contact Line Motion at all Scales. *Phys. Rev. Lett.* **116**, 184502, (2016).  
 291 35 Huang, K. & Szlufarska, I. Green-Kubo relation for friction at liquid-solid interfaces. *Phys. Rev.*  
 292 *E* **89**, 032119, (2014).  
 293 36 Daniel, D., Timonen, J. V. I., Li, R., Velling, S. J. & Aizenberg, J. Oleoplaning droplets on  
 294 lubricated surfaces. *Nat. Phys.* **advance online publication**, (2017).  
 295 37 Butt, H.-J. *et al.* Energy Dissipation of Moving Drops on Superhydrophobic and  
 296 Superoleophobic Surfaces. *Langmuir* **33**, 107-116, (2017).  
 297 38 Israelachvili, J. N. *Intermolecular and Surface Forces*. (Elsevier Science, 2011).  
 298 39 Butt, H.-J. & Kappl, M. *Surface and Interfacial Forces*. (Wiley, 2010).



301  
 302 **Figure 1 | Schematics of friction force measurements.** **a**, Textbook configuration for demonstrating  
 303 solid–solid friction. **b**, Homemade setup for measuring liquid–solid friction. A drop of liquid is placed  
 304 on a solid substrate mounted on a linear stage driven by a step motor. A laser beam incident on the  
 305 capillary is reflected to a position-sensitive detector (PSD). The contact width between the drop of  
 306 liquid and the solid surface (orthogonal to the direction of motion) and contact length (parallel to the  
 307 direction of motion) are simultaneously monitored by cameras (not shown).



310  
 311 **Figure 2| Lateral adhesion force experiment of a drop of ionic liquid (volume  $\approx 1.5 \mu\text{L}$ ) on a**  
 312 **fluorinated Si wafer.** The measurement was performed at a constant linear stage velocity of  $200 \mu\text{m/s}$ .  
 313 The surface tension of the ionic liquid 1-butyl-2,3-dimethylimidazolium  
 314 bis(trifluoromethanesulfonyl)imide is  $34.6 \text{ mN/m}$ . **a**, The measured lateral adhesion force is plotted  
 315 with blue circles. The error in force measurement is  $\pm 1 \mu\text{N}$  and smaller than the symbol size. The  
 316 calculated force is plotted with red squares. **b**, Simultaneously determined contact width and length  
 317 of the drop during the force measurement shown in **a**. **c**, Front and rear contact angles during the force  
 318 measurement. Movie 1 shows the motion of the ionic liquid drop on the fluorinated Si wafer during  
 319 the lateral adhesion force measurement.

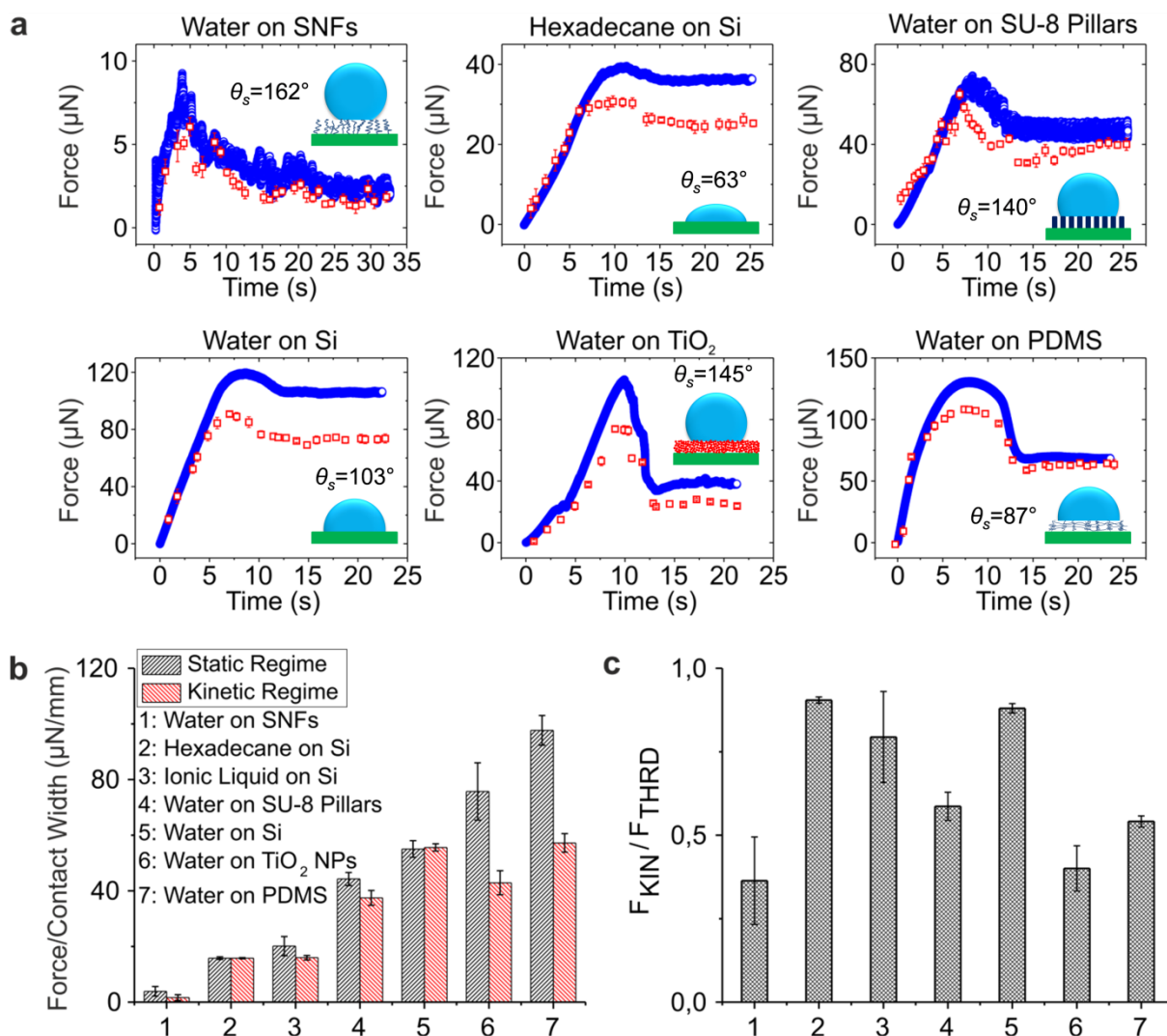
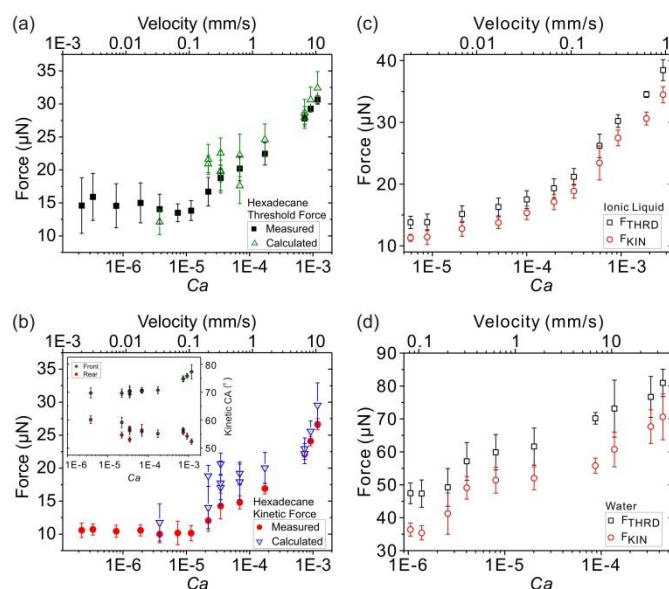
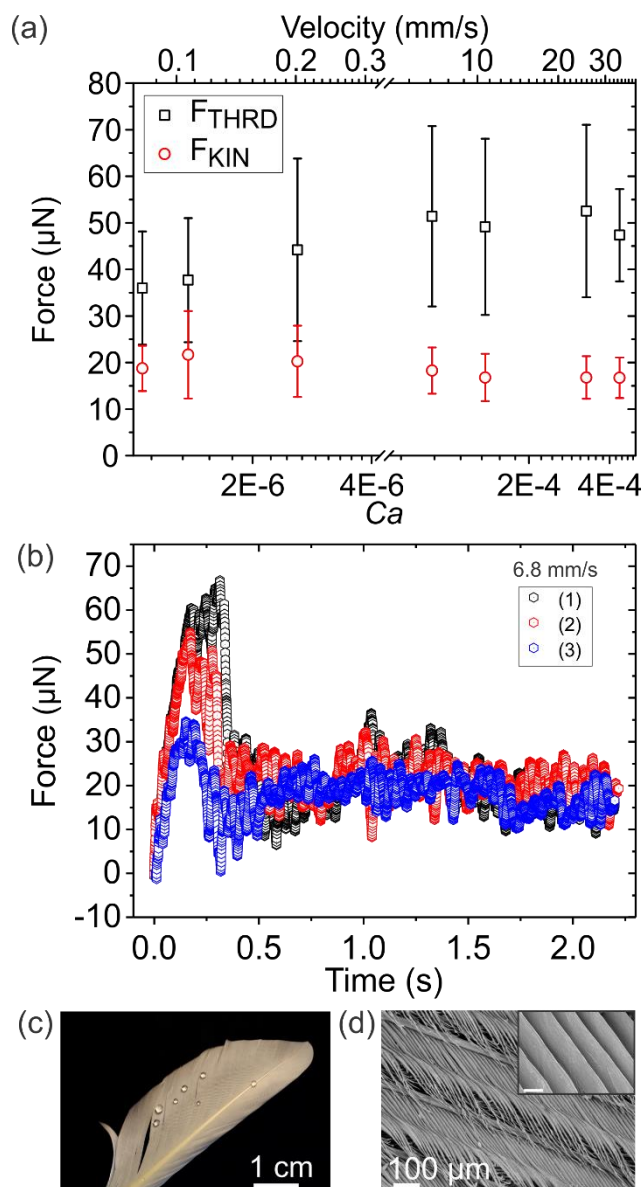


**Figure 3 | Lateral adhesion forces for drops of different liquids on solid surfaces.** **a**, Measured (blue circles) and calculated lateral adhesion forces using  $k = 1$  (red squares). The surfaces include silicone nanofilaments (SNFs), silicon wafers (Si), SU-8 square pillar arrays (height:  $25 \mu\text{m}$ , width:  $50 \mu\text{m}$ , centre–centre distance:  $100 \mu\text{m}$ ), multilayers of 20-nm titanium dioxide nanoparticles ( $\text{TiO}_2$  NPs), and cross-linked polydimethylsiloxane (PDMS). All surfaces except for those of polydimethylsiloxane were fluorinated before use. All fabrication details are provided in the online methods section. The adopted surface tensions of water and hexadecane are  $73.5 \text{ mN}/\text{m}$  and  $27.5 \text{ mN}/\text{m}$  at room temperature, respectively. The advancing and receding contact angles were  $171 \pm 1^\circ$  and  $164 \pm 1^\circ$  for water on fluorinated silicone nanofilaments,  $83 \pm 1^\circ$  and  $59 \pm 1^\circ$  for hexadecane on fluorinated silicon wafers,  $169 \pm 2^\circ$  and  $122 \pm 2^\circ$  for water on fluorinated SU-8 pillars,  $128 \pm 1^\circ$  and  $95 \pm 1^\circ$  for water on fluorinated silicon wafers,  $164 \pm 1^\circ$  and  $128 \pm 2^\circ$  for water on titanium dioxide nanoparticles, and  $121 \pm 1^\circ$  and  $81 \pm 1^\circ$  for water on cross-linked PDMS, respectively (Supplementary Figs. 5–10). Movies 2–7 show the motions of drops on the different surfaces during the lateral adhesion force measurements. **b**, Lateral adhesion force per unit contact width. Drop volumes between  $1.5$  and  $8 \mu\text{L}$  were chosen to avoid

337 rupturing of drops during motion. **c**, Ratios of the kinetic friction force  $F_{\text{KIN}}$  and its threshold force  $F_{\text{THRD}}$   
 338 of all liquid–solid combinations that are studied. Here we used  $F_{\text{KIN}}$  and  $F_{\text{THRD}}$  prior normalization with  
 339 the respective contact widths in order to point out  $F_{\text{KIN}}/F_{\text{THRD}} \leq 1$ . Error bars in b and c indicate variability  
 340 between different experiments.



341  
 342 **Figure 4 | Velocity dependence of lateral adhesion forces.** Development of the lateral adhesion force  
 343 of hexadecane drops ( $\approx 3 \mu\text{L}$ ) on a fluorinated Si wafer surface (a) at threshold and (b) in the kinetic  
 344 regime. The inset shows the front and rear contact angles measured in the kinetic regime. (c) Velocity  
 345 dependence of lateral adhesion forces of an ionic liquid (1-butyl-2,3-dimethylimidazolium  
 346 bis(trifluoromethanesulfonyl)imide) drop ( $\approx 2 \mu\text{L}$ ) on a fluorinated Si wafer substrate and (d) water  
 347 drops ( $\approx 7.5 \mu\text{L}$ ) on a fluorinated Si wafer substrate. Here velocities below  $0.08 \text{ mm/s}$  were not studied  
 348 owing to evaporation of water. The error bars correspond to the standard deviation calculated from 5  
 349 - 7 independent measurements. The highest velocity that can be probed is given by the threshold force  
 350 where the liquid drop detaches from the glass capillary ( $\approx 81 \mu\text{N}$  for water,  $\approx 36 \mu\text{N}$  for ionic liquid and  
 351  $\approx 31 \mu\text{N}$  for hexadecane).



352

353

354

355

356

357

358

359

360

361

**Figure 5 | Lateral adhesion force measurement of a water drop on a goose feather (a)** at threshold (black squares) and in the kinetic regime (red circles). The error bars correspond to the standard deviations calculated from 5 - 7 measurements each. **(b)** Three different lateral adhesion force measurement of a water drop on a goose feather at different areas at a velocity of 6.8 mm/s (drop volume of 8 μL). The threshold lateral adhesion force varied between  $35 \pm 1 \mu\text{N}$  and  $67 \pm 2 \mu\text{N}$ . Continuing the kinetic motion of the water drop required a force up to 35 μN. **(c)** An optical image of the feather with resting water drops. **(d)** Scanning electron microscopy images reveal the detailed structure of the feather. The inset is an enlarged area of (c) showing the microscopic structure. The scale bar in the inset is 10 μm.